

Pattern formation in oil-in-water emulsions exposed to a salt gradientYing Liu,¹ Bhargav Rallabandi,^{2,1} Lailai Zhu,^{1,3} Ankur Gupta,¹ and Howard A. Stone^{1,*}¹*Department of Mechanical and Aerospace Engineering, Princeton University,
Princeton, New Jersey 08544, USA*²*Department of Mechanical Engineering, University of California,
Riverside, California 92521, USA*³*Linné Flow Centre and Swedish e-Science Research Centre (SeRC),
KTH Mechanics, SE-10044 Stockholm, Sweden*

(Received 3 November 2018; published 30 August 2019)

Flow instabilities can occur in a fluid system with two components that have significantly different diffusivities and that have opposite effects on the fluid density, as is the scenario in traditional double-diffusive convection. Here, we experimentally show that an oil-in-water emulsion exposed to salt concentration gradients generates a flowerlike pattern driven by vertical and azimuthal instabilities. We also report numerical and analytical studies to elaborate on the mechanism, the instability criteria, and the most unstable modes that determine the details of the observed patterns. We find that the instability is driven by buoyancy and stems from the differential transport between the dissolved salt and the suspended oil droplets, which have opposing effects on the density of the medium. Consequently, we identify a criterion for the development of the instability that involves the relative densities and concentrations of the salt and oil droplets. We also argue that the typical wave number of the pattern formed scales with the Péclet number of the salt, which here is equivalent to the Rayleigh number since the flow is driven by buoyancy. We find good agreement of these predictions with both experiments and numerical simulations.

DOI: [10.1103/PhysRevFluids.4.084307](https://doi.org/10.1103/PhysRevFluids.4.084307)**I. INTRODUCTION**

Pattern formation induced by instabilities of fluid flows occurs in many systems [1–4]. Not only are they common in nature, e.g., the fluctus clouds formed by the Kelvin-Helmholtz instability [5], von Kármán vortex streets in clouds [6], and the crown splash formed by the Rayleigh-Plateau instability [7], but similar instabilities also occur in applications such as spin coating [8,9], fabrication of multiple-layered structures [10], and enhanced heat transfer [11]. Flow-driven instability and pattern formation in both single-phase and multiphase flow systems have been studied widely [12–16]. Recently, the instability in multiphase miscible systems with dissolution-driven convection has been discussed (e.g., applications in CO₂ sequestration) [17–19]. However, the corresponding dynamics in a multiphase miscible system, where diffusion-driven effects occur, is less discussed and is one of the motivations for the present work.

The other motivation of the current study is that in many multicomponent fluid systems, a variety of fluid dynamic regimes arise since the fluid properties change with the composition of the system. For instance, in some gravity currents propagating below an ambient fluid, dense particles can be present in the current. In such scenarios, sedimentation of the particles changes the effective density of the medium, which can become lower than the ambient, i.e., the effective buoyancy is reversed

*hastone@princeton.edu

and a plume is thus observed at late times [20,21]. As another example, the thermal and solutal Marangoni flows during the multicomponent evaporation of sessile Ouzo drops spontaneously emulsify the liquids in the drops [22].

Some of the most widespread multicomponent fluid systems are emulsions, which are present in various applications, and often these systems have a wide range of chemicals, e.g., salts, present. In such cases, the droplets in the emulsion and the salt both contribute to changes in the fluid density. Here, we show that when an oil-in-water emulsion with a high salt concentration in its aqueous phase is injected into a horizontally oriented Hele-Shaw cell filled with a salt solution at a low concentration, the drop spreads and a three-dimensional pattern of the emulsion appears, which resembles a flower shape, due to the diffusion of the salt.

In the experiments we report, the emulsion with a high salt concentration in its aqueous phase was initially denser than the ambient fluid. Due to the diffusion of salt from the emulsion into the surrounding liquid [23], the spreading current of emulsion became increasingly buoyant over time. Consequently, the system became unstably stratified, which forced the lighter emulsion phase to rise towards the top of the Hele-Shaw cell and overturn. This phenomenon is similar to double-diffusive convection [10,24–28], where there are two competing components to change the fluid density and influence the flow, including potentially driving an instability: for the current work, oil decreased and salt increased the density; for double-diffusive convection, heat decreases and salt increases the density. Our work sheds light upon systems closely related to oil/water emulsions, so we anticipate that similar phenomena may occur in many engineered flow processes.

II. EXPERIMENTS

A. Materials

Silicone oil of viscosity $\mu_o = 9.7 \times 10^2$ cP and density $\rho_o = 0.97$ g/mL, sodium chloride, and Span-80 were obtained from Sigma-Aldrich. Tween-80 was purchased from EM Science. TP-3400 from Tracer Products was used as an oil-based fluorescent dye. Deionized water with electrical conductivity $\sigma = 5.4$ μ S/m was used for all the aqueous phases. The material properties have values based on the typical conditions of 25 °C and 1 atm.

B. Emulsion preparation

An oil-in-water emulsion was prepared before each experiment. The oil phase consisted of silicone oil and fluorescent dye at the ratio of 19:1, by volume, and the aqueous phase was a sodium chloride solution with molar concentration c_{em} , with a typical value $c_{em} = 100$ mM. Nonionic surfactants Span-80 and Tween-80 were both used as emulsifiers to avoid electrolyte screening effects [29,30]. To prepare the emulsion, the oil phase was added into the aqueous phase at the ratio 1:9, by volume. The surfactants were added to this mixture: 0.03 wt% for Span-80 and 0.3 wt% for Tween-80. Next, the solution was mixed well by using an ultrasonic dismembrator (Model 150E; Fisher Scientific) for 5 min at 150 W output power, after which the emulsion was left standing at room temperature (25 °C) for 1 h. We used the lower layer of the emulsion for the flow experiments to exclude the large oil droplets that rose to the upper layer. The volume fraction of the oil phase in the emulsion is denoted $\phi_0 \approx 0.1$. Finally, the external fluid used in the flow experiment was a sodium chloride solution with concentration c_{ext} , with a typical value $c_{ext} = 1$ mM.

To evaluate the size of the emulsion droplets, the emulsion was observed using a confocal microscope (Leica SP5) and the droplet sizes were extracted from microscope images using ImageJ. We found that the diameters of the oil droplets were $d = 10 \pm 5$ μ m. The viscosity of the emulsion was $\mu_{em} = 1.09 \pm 0.01$ mPa \cdot s, as measured by a rheometer (Anton Paar MCR 301). Other parameters of the emulsion important in this study are also mentioned here: the diffusion coefficient of the sodium chloride in water was $D_s \simeq 1.6 \times 10^{-9}$ m² s⁻¹ [31]. The diffusion coefficient of the oil droplets in water was $D_o = 1.1 \times 10^{-13}$ m² s⁻¹, which was calculated from the Stokes-Einstein equation [32] with average droplet diameter $d = 10$ μ m. Since the pattern formation we observed

was induced by the density gradient caused by the salt and the oil droplets (as documented in Sec. IV B), we describe the effects of these two components on the fluid density, respectively, by the two positive expansion coefficients

$$\beta_o \equiv \frac{\rho_w - \rho_o}{\rho_w}, \quad (1a)$$

$$\beta_s \equiv \frac{M_s}{\rho_w}, \quad (1b)$$

where $M_s = 5.84 \times 10^{-2}$ kg/mol is the molar mass of sodium chloride. The density of the fluid with salt concentration c and oil volume fraction ϕ relative to water can be written as

$$\Delta\rho = \rho_w[(1 - \phi)\beta_s c - \beta_o\phi], \quad (2)$$

where $\rho_w = 1.0 \times 10^3$ kg/m³ is the density of water. Note that 1 mM = 1 mol/m³, so that all the products in Eq. (2) have the same units. It can be seen that the salt increases the density, while the oil decreases it. The relative density of the emulsion with $c_{\text{em}} = 100$ mM and $\phi = \phi_0$, using Eqs. (1a), (1b), and (2), was $\Delta\rho_{\text{em}} = 3.0$ kg/m³. The relative density of the external fluid in our experiments, i.e., sodium chloride solution with concentration $c_{\text{ext}} = 1$ mM and $\phi = 0$, using Eqs. (1a), (1b), and (2), was $\Delta\rho_{\text{ext}} = 6.0 \times 10^{-2}$ kg/m³. We adjusted c_{em} and c_{ext} to change $\Delta\rho_{\text{em}}$ and $\Delta\rho_{\text{ext}}$, which led to different flow features and a different pattern formation of the emulsion.

C. Flow cell fabrication

The experiment was conducted in a horizontally oriented, square Hele-Shaw cell of height $H = 500 \pm 50$ μm and side length $L = 18$ mm [see Fig. 1(a)]. To fabricate the cell, we first mixed polydimethylsiloxane (PDMS) with a cross-linking agent at the ratio of 10:1, by mass, then poured the mixture into a petri dish to form a thin layer, about 0.5 mm thick, and cured it at 75 °C for 2.5 h. Next, we cut a hollow square of outer side length $L = 22$ mm and inner side length $L = 18$ mm from the PDMS layer. A small outlet was also cut into the PDMS. The PDMS was corona treated (Electro-Technic Products Inc.) for 30 s on both sides and sandwiched between two pieces of identical cover glass. To finish bonding, the channel was heated at 150 °C for 15 min and then cooled at room temperature. The height of the channel was measured using a confocal microscope (Leica SP5) and a reflective channel.

D. Pattern formation

We first filled the Hele-Shaw cell with the external fluid, i.e., sodium chloride solution with salt concentration c_{ext} , and then used a needle to inject a small drop of the oil-in-water emulsion with a volume of about 1.6 μL and $\phi_0 \approx 0.1$ [see Fig. 1(a)]. At this moment, the initial density of the emulsion is higher than that of the external salt solution by 2.9 kg/m³ as estimated by Eq. (2). The needle was withdrawn and the evolution of the emulsion was observed using a confocal microscope (Nikon A1R HD). Initially, the emulsion had the shape of a cylinder with radius $a \approx 1.0$ mm spanning the gap of the Hele-Shaw cell [see Fig. 1(b)]. When the emulsion was denser than the external fluid, i.e., $\Delta\rho_{\text{em}} > \Delta\rho_{\text{ext}}$ ($c_{\text{em}} = 100$ mM and $c_{\text{ext}} = 1$ mM), the emulsion spread at the bottom of the cell. Subsequently, we observed an instability that produced a pattern of the emulsion (see the video in the Supplemental Material [33]). As we show, this pattern formation can be understood as being produced by the diffusion of salt from the emulsion into the external solution. The final pattern of the emulsion was reached after about 280 s as shown in Fig. 1(c). In contrast, when the emulsion was initially less dense than the external fluid by 2.9 kg/m³, as estimated by Eq. (2), i.e., $\Delta\rho_{\text{em}} < \Delta\rho_{\text{ext}}$ ($c_{\text{em}} = c_{\text{ext}} = 1$ mM), the emulsion spread stably at the top of the cell and the final pattern obtained is shown in Fig. 1(d). It turns out that an unstable density gradient occurred in the former case, whereas the density gradient was always stable in the latter case. We

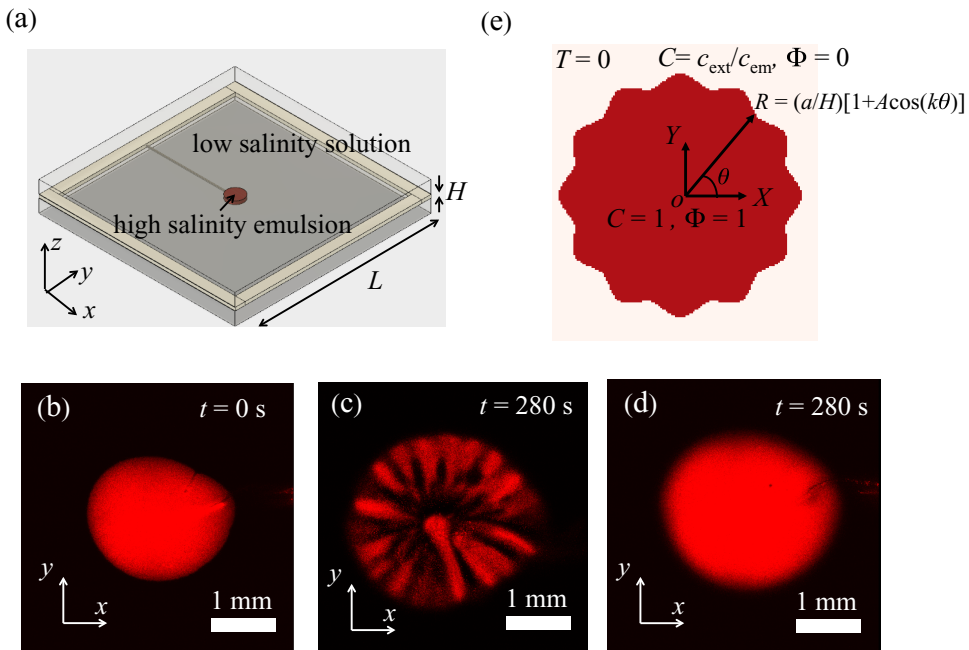


FIG. 1. (a) Sketch of the experimental setup: a drop of dyed oil-in-water emulsion with sodium chloride concentration c_{em} in the aqueous phase and oil volume fraction ϕ_0 was injected using a needle into a Hele-Shaw cell filled with a sodium chloride solution with salt concentration c_{ext} . The needle was then withdrawn, leaving the drop of emulsion, which flowed and formed a pattern. (b) Top view of the initial state of the emulsion (red area) in experiments at $t = 0$ s. (c) Top view of the final state of the unstable emulsion pattern in experiments at $t = 280$ s when the emulsion was initially denser than the external fluid, i.e., $\Delta\rho_{em} > \Delta\rho_{ext}$ ($c_{em} = 100$ mM and $c_{ext} = 1$ mM). (d) Top view of the final state of the stable emulsion pattern in experiments at $t = 280$ s when the emulsion was initially less dense than the external fluid, i.e., $\Delta\rho_{em} < \Delta\rho_{ext}$ ($c_{em} = c_{ext} = 1$ mM). (e) Top view of the initial condition with an azimuthal perturbation with amplitude $A = 0.1$ and wave number $k = 12$ for the numerical simulation. The red area represents an emulsion with oil volume fraction $\Phi = 1$ and dimensionless salt concentration $C = 1$ in the aqueous phase, and the white background represents the external fluid with oil volume fraction $\Phi = 0$ and dimensionless salt concentration $C = c_{ext}/c_{em}$.

focus in the rest of the paper on conditions where $\Delta\rho_{em} > \Delta\rho_{ext}$ so that there is the occurrence of an instability. The mechanism of the instability is illustrated and discussed in Sec. IV B.

III. NUMERICAL SIMULATIONS

A. Dimensional equations

In order to understand the pattern formation of the two-phase emulsion, we conducted three-dimensional simulations using the solvers provided by the BASILISK code [34], which employs the finite-volume method to solve the governing equations. We assumed that the viscosity was approximately equal to the viscosity of the water for these relatively dilute systems, i.e., $\mu_{em} \approx \mu_w$. The octree grids were utilized, and the middle of the simulation domain, within which the emulsion formed patterns, was refined. The governing equations, based on the Boussinesq approximation,

were

$$\nabla \cdot \mathbf{u} = 0, \quad (3a)$$

$$\rho_w \left(\frac{\partial \mathbf{u}}{\partial t} + \mathbf{u} \cdot \nabla \mathbf{u} \right) = -\nabla p + \mu_w \nabla^2 \mathbf{u} + [\beta_o \phi - (1 - \phi) \beta_s c] \rho_w g \mathbf{e}_z, \quad (3b)$$

$$\frac{\partial c}{\partial t} + \mathbf{u} \cdot \nabla c = D_s \nabla^2 c, \quad (3c)$$

$$\frac{\partial \phi}{\partial t} + \mathbf{u} \cdot \nabla \phi = D_o \nabla^2 \phi, \quad (3d)$$

where \mathbf{u} is the fluid velocity and μ_w is the viscosity of the water. Equations (3a)–(3d) are, respectively, the continuity equation for an incompressible flow, the Navier-Stokes equations, and the advection-diffusion equations for salt concentration c and oil volume fraction ϕ .

A cylindrical volume of emulsion with azimuthal perturbations in c and ϕ , with wave number k and amplitude A , was introduced in the initial condition [see Fig. 1(e)]. Introducing the polar coordinates (r, θ) defined in the (x, y) plane,

$$x \equiv r \cos \theta, \quad (4a)$$

$$y \equiv r \sin \theta, \quad (4b)$$

the initial conditions (for $|z| < H/2$) were

$$\mathbf{u} = \mathbf{0}, \quad \text{all } r, \theta, z, \quad (5a)$$

$$c = \begin{cases} c_{\text{em}} & \text{if } 0 \leq r \leq a[1 + A \cos(k\theta)], \quad \text{all } \theta, z, \\ c_{\text{ext}} & \text{if } r > a[1 + A \cos(k\theta)], \quad \text{all } \theta, z, \end{cases} \quad (5b)$$

$$\phi = \begin{cases} \phi_0 & \text{if } 0 \leq r \leq a[1 + A \cos(k\theta)], \quad \text{all } \theta, z, \\ 0 & \text{if } r > a[1 + A \cos(k\theta)], \quad \text{all } \theta, z. \end{cases} \quad (5c)$$

The boundary conditions on the top and bottom walls of the Hele-Shaw cell were no slip, i.e.,

$$\mathbf{u}(r, \theta, z = \pm H/2) = \mathbf{0}, \quad (6)$$

with no flux of salt and oil droplets, i.e.,

$$\left. \frac{\partial c}{\partial z} \right|_{z=\pm H/2} = 0, \quad (7a)$$

$$\left. \frac{\partial \phi}{\partial z} \right|_{z=\pm H/2} = 0. \quad (7b)$$

B. Dimensionless equations

The problem can be nondimensionalized by the characteristic values (subscript c)

$$\ell_c = H, \quad (8a)$$

$$u_c = \frac{\phi_0 \beta_o H^2 g}{\nu}, \quad (8b)$$

$$t_c = \frac{\nu}{\phi_0 \beta_o H g}, \quad (8c)$$

$$c_c = c_{\text{em}}, \quad (8d)$$

$$\phi_c = \phi_0, \quad (8e)$$

$$p_c = \frac{\rho_w \phi_0^2 \beta_o^2 H^4 g^2}{\nu^2}, \quad (8f)$$

where $\nu = \mu_w/\rho_w$ is the kinematic viscosity of water. Thus, with

$$\nabla^* \equiv \ell_c \nabla, \quad (9a)$$

$$R \equiv \frac{r}{\ell_c}, \quad (9b)$$

$$Z \equiv \frac{z}{\ell_c}, \quad (9c)$$

$$\mathbf{U} \equiv \frac{\mathbf{u}}{u_c}, \quad (9d)$$

$$T \equiv \frac{t}{t_c}, \quad (9e)$$

$$C \equiv \frac{c}{c_c}, \quad (9f)$$

$$\Phi \equiv \frac{\phi}{\phi_c}, \quad (9g)$$

$$P \equiv \frac{P}{P_c}, \quad (9h)$$

we obtain the dimensionless governing equations

$$\nabla^* \cdot \mathbf{U} = 0, \quad (10a)$$

$$\frac{\partial \mathbf{U}}{\partial T} + \mathbf{U} \cdot \nabla^* \mathbf{U} = -\nabla^* P + \text{Re}^{-1} \nabla^{*2} \mathbf{U} + (\text{Re}^{-1} \Phi - \text{Re}^{-1} \alpha_{s,o} (1 - \phi_0 \Phi) C) \mathbf{e}_z, \quad (10b)$$

$$\frac{\partial C}{\partial T} + \mathbf{U} \cdot \nabla^* C = \text{Pe}_s^{-1} \nabla^{*2} C, \quad (10c)$$

$$\frac{\partial \Phi}{\partial T} + \mathbf{U} \cdot \nabla^* \Phi = \text{Pe}_o^{-1} \nabla^{*2} \Phi. \quad (10d)$$

Here, Re is the Reynolds number, Pe_s and Pe_o are the Péclet numbers of salt and oil droplets, respectively, and $\alpha_{s,o}$ is the ratio of the relative density of the emulsion due to the salt concentration to that due to the oil volume fraction, which are given by

$$\text{Re} \equiv \frac{\phi_0 \beta_o H^3 g}{\nu^2}, \quad (11a)$$

$$\text{Pe}_s \equiv \frac{\phi_0 \beta_o H^3 g}{\nu D_s}, \quad (11b)$$

$$\text{Pe}_o \equiv \frac{\phi_0 \beta_o H^3 g}{\nu D_o}, \quad (11c)$$

$$\alpha_{s,o} \equiv \frac{\beta_s c_{em}}{\beta_o \phi_0}. \quad (11d)$$

We note that Re as defined here is commonly called the Grashof number [35–37], while Pe_s and Pe_o are the Rayleigh numbers based on the corresponding diffusivities. The dimensionless initial conditions are [see Fig. 1(e)] ($|Z| < 1/2$)

$$\mathbf{U} = \mathbf{0}, \quad \text{all } R, \theta, Z, \quad (12a)$$

$$C = \begin{cases} 1 & \text{if } 0 \leq R \leq (a/H)[1 + A \cos(k\theta)], \quad \text{all } \theta, Z, \\ c_e/c_i & \text{if } R > (a/H)[1 + A \cos(k\theta)], \quad \text{all } \theta, Z, \end{cases} \quad (12b)$$

$$\Phi = \begin{cases} 1 & \text{if } 0 \leq R \leq (a/H)[1 + A \cos(k\theta)], \quad \text{all } \theta, Z, \\ 0 & \text{if } R > (a/H)[1 + A \cos(k\theta)], \quad \text{all } \theta, Z. \end{cases} \quad (12c)$$

TABLE I. The dimensionless parameters and their typical values in the numerical simulations, which are consistent with experiments with $c_{\text{em}} = 100$ mM and $c_{\text{ext}} = 1$ mM.

Dimensionless parameter							
Re	Pe_s	Pe_o	$\alpha_{s,o}$	a/H	$c_{\text{em}}/c_{\text{ext}}$	k	A
2.5	1.6×10^3	2.5×10^7	2.9	1	1.0×10^2	12	0.1

The dimensionless boundary conditions are

$$U(R, \theta, Z = \pm 1/2) = \mathbf{0}, \quad (13a)$$

$$\left. \frac{\partial C}{\partial Z} \right|_{Z=\pm 1/2} = 0, \quad (13b)$$

$$\left. \frac{\partial \Phi}{\partial z} \right|_{Z=\pm 1/2} = 0. \quad (13c)$$

$$(13d)$$

The dimensionless parameters and their typical values used in the numerical simulations are listed in Table I; the values are consistent with the experiments with $c_{\text{em}} = 100$ mM and $c_{\text{ext}} = 1$ mM. While keeping Re, Pe_o , a/H , and A fixed, we changed Pe_s , $\alpha_{s,o}$, and $c_{\text{em}}/c_{\text{ext}}$ to study their influence on the instability/pattern formation. Different wave numbers k were also imposed with the same sets of the other dimensionless parameters in order to extract the most unstable mode based on the growth rate of the instability defined later in Sec. IV D. In the rest of the paper, the values of the dimensionless parameters are the same as those in Table I except where stated otherwise. Since $Pe_o \gg Pe_s$, i.e., the diffusion of the oil droplets was negligible [see Eq. (10d)] compared with the convection driven by the density gradient, and so the oil droplets can be considered passive tracers of the flow, i.e., they followed the motion of the fluid. Therefore, the emulsion/aqueous boundary $\Phi = 1$ was a streakline in the flow, and the fingering pattern represented the instability of the flow.

The dynamics of pattern formation, i.e., the time evolution of the emulsion/aqueous boundary $\Phi = 1$ in a numerical simulation with parameters listed in Table I, are shown in Fig. 2(a) at $T = 30$, in Fig. 2(b) at $T = 90$, and in Fig. 2(c) at $T = 150$ (see the video in the Supplemental Material [38]). The results show that the emulsion first spread at the bottom of the cell without obvious enhancement of the fingering [see Fig. 2(a)], then the emulsion curled upward at radius $R \approx 1.6$ [see Fig. 2(b)], and, finally, the leading edge moved inwards and the fingering grew significantly [see Fig. 2(c)].

IV. RESULTS AND DISCUSSION

A. Comparison of the experimental and the simulation results

The results of the experiments and the numerical simulations are compared in this section. For consistency, all of the dimensionless parameters in the numerical simulation in Table I were calculated with Eq. (11a)–(11d) using the experimental parameters, except that we imposed the azimuthal wave number k and amplitude A . The good qualitative agreement between the computational and the experimental results is shown in Fig. 2 (see also the videos in the Supplemental Material [33,38]). In the experiments with both $c_{\text{em}} = 100$ mM and $c_{\text{ext}} = 1$ mM and the numerical simulations with consistent dimensionless parameters (values in Table I), the emulsion first spread along the bottom and then curled upward. The fingering developed radially inwards at late times (see the videos in the Supplemental Material [33,38]). The top [see Fig. 2(d)] and side [see Fig. 2(e)] views of the final three-dimensional structure of the emulsion fingering observed with the confocal microscope are similar to the time evolution in the numerical simulation [see Fig. 2(c)].

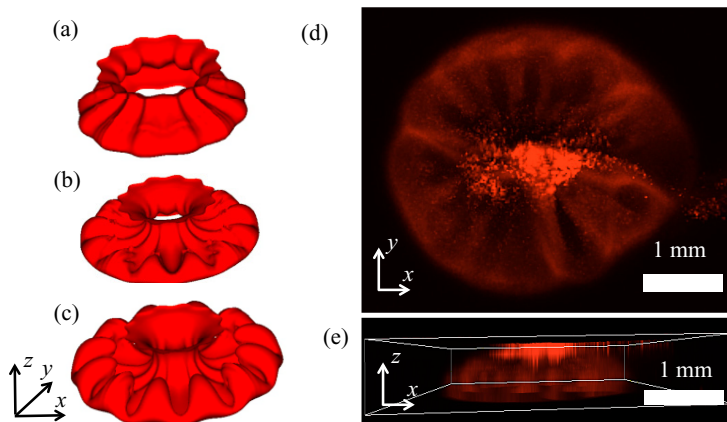


FIG. 2. Comparison of the three-dimensional structure of the emulsion pattern in numerical simulations (a)–(c) and experiments (d), (e). (a)–(c) Snapshots of the three-dimensional structure of the fingering in a numerical simulation with dimensionless parameters of values listed in Table I at $T = 30$ (a), $T = 90$ (b), and $T = 150$ (c). (d), (e) Images from an experiment with $c_{em} = 100$ mM and $c_{ext} = 1$ mM of the top (d) and side (e) views of the three-dimensional structure of the emulsion pattern taken using a confocal microscope at $t = 280$ s (final state).

In particular, top views of the emulsion pattern in the experiments and the numerical simulations are compared in Fig. 3 to emphasize the azimuthal instability. The top views of the fingering in experiments with $c_{em} = 100$ mM and $c_{ext} = 1$ mM are shown in Figs. 3(a)–3(c). We note that even though the experimental images were taken at a particular confocal plane at a depth about $140 \mu\text{m}$ from the top, the similar emulsion patterns were also observed in a depth-averaged view taken with a regular camera. Therefore, the depth-averaged oil volume fraction $\bar{\Phi} = \int_{-1/2}^{1/2} \Phi dZ$ [see Figs. 3(d)–3(f)] in the numerical simulations with consistent dimensionless parameters (values in Table I) was chosen to compare with the experimental results [see Figs. 3(a)–3(c)]. We observe that at the early times when the emulsion spread along the bottom, the fingering pattern was weak in both the experiment [see Fig. 3(a)] and the simulation [see Fig. 3(d)]. Even though in the numerical simulation, $\bar{\Phi}$ was higher at the angle corresponding to the peaks of the initial perturbation, i.e., $\theta = 2n\pi/k$, than at the angle corresponding to the valleys of the initial perturbation, i.e., $\theta = (2n + 1)\pi/k$, where $n \in \{0, 1, \dots, k - 1\}$, the difference in $\bar{\Phi}$ between the peak and the valley was small, which is shown by the much weaker azimuthal color contrast in Fig. 3(d) compared with Figs. 3(e) and 3(f). The slight accumulation of the oil droplets at the peak can also be seen from the ridges in the three-dimensional view in Fig. 2(b). However, after the emulsion curled upward, both the experiments [see Figs. 3(b) and 3(c)] and the simulation [see Figs. 3(e) and 3(f)] showed obvious fingering, which grew towards the center. This means that there was azimuthal instability driving the oil droplets to accumulate towards the peaks from the valleys. The three-dimensional view in the numerical simulation [see Fig. 2(c)] and experimental video (see also the video in the Supplemental Material [33]) further illustrates that the fingering occurred at the top of the flow cell. Finally, the time scale associated with the experiments in Fig. 3 was such that the simulations (which utilized $a/H = 1$) evolved more rapidly than the experiments (for which $a/H \simeq 2$); we believe that these geometric changes influenced the time scales of the long, narrow gravity currents.

B. The mechanism of the instability

When the emulsion was denser than the external fluid, i.e., $\Delta\rho_{em} > \Delta\rho_{ext}$, it flowed as a gravity current at the bottom of the Hele-Shaw cell [23,39,40]. In this case, the emulsion also had a

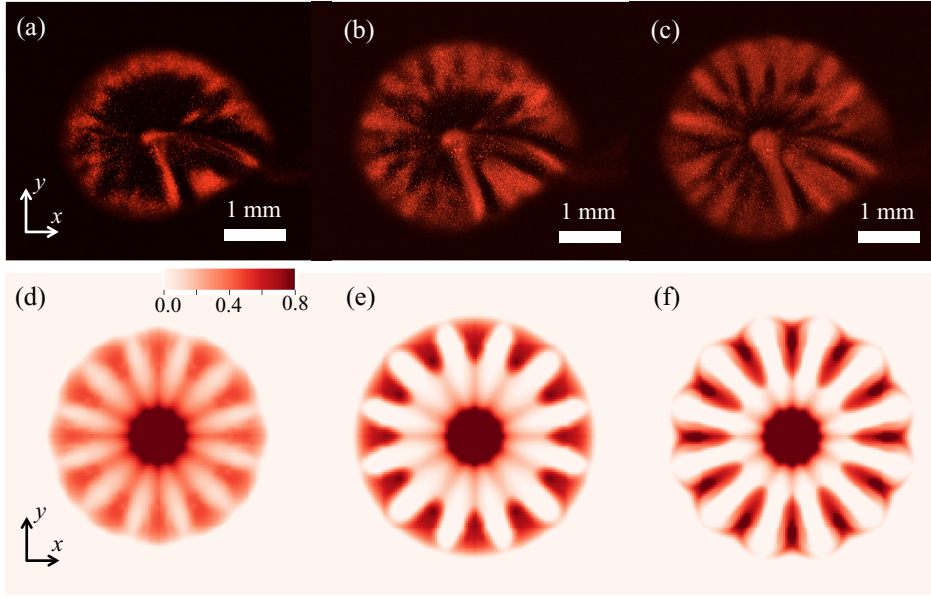


FIG. 3. Comparison of the evolution of the top views of the emulsion pattern in experiments (a)–(c) and numerical simulations (d)–(f). (a)–(c) Top views of the emulsion pattern in experiments with $c_{em} = 100$ mM and $c_{ext} = 1$ mM at $t = 140$ s (a), $t = 210$ s (b), and $t = 280$ s (c). (d)–(f) Top views of the depth-averaged oil volume fraction $\bar{\Phi}$ in a numerical simulation with dimensionless parameters (Table I) at $T = 90$ (d), $T = 150$ (e), and $T = 210$ (f). The characteristic time $t_c \approx 0.1$ s is obtained using Eq. 8(e).

significantly higher salt concentration than the external fluid. Then, as the salt, with dimensionless concentration C , diffused more rapidly than the oil droplets, with volume fraction Φ , the bottom layer of the fluid, which contained oil droplets, spread and progressively became less dense than the upper layer of fluid [see Eq. (2)]. Therefore, an instability occurred (see the video in the Supplemental Material [33]). The dynamics of this flow are similar to the phenomenon of double-diffusive convection [10,24–28], where salty and warmer water on top of fresh and cooler water produces salt fingers. Both in our experiments and in double-diffusive convection, there are two components with distinct diffusion coefficients and opposite effects on the fluid density. In particular, in our experiments, salt, which increased the fluid density, diffused much more rapidly than the oil droplets, which decreased the fluid density [see Eq. (2)]. In the double-diffusive convection, heat, which decreases the fluid density, diffuses much more rapidly than the salt, which increases the fluid density. This contrast in diffusivities introduced a transition of the vertical density gradient from stable to unstable.

The vertical convection observed in the flow in our experiments is shown in Fig. 4(a). However, in the confined axisymmetric geometry in the current study, we observed an azimuthal instability, which is not typically observed in the conventional double-diffusive convection. We show that both the azimuthal instability and the double-diffusive convection together drove a secondary flow [see Fig. 4(b)], which generated the instability and pattern formation of the emulsion.

In order to better understand the vertical instability, we looked at vertical cross sections through the origin (R, Z) plane in the numerical simulation at the peak $\theta = 0$ [see Figs. 5(a), 5(c), 5(e)] and at the valley $\theta = \pi/12$ [see Figs. 5(b), 5(d), 5(f)]. Both the velocity fields (vectors) and the emulsion/water boundary (red curve), i.e., $\Phi = 1$, are shown at $T = 30, 120$, and 210 . There are two features of note: first, the oil tended to be depleted at the valley and accumulated towards the peak, which can be seen by the change in the area surrounded by the emulsion/water boundary (red curve); second, the fingering only occurred at the peak angles of the initial perturbation. At

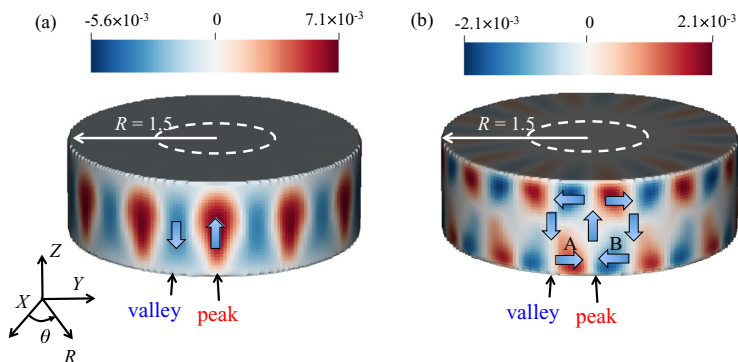


FIG. 4. Secondary flows at $R = 1.5$ and $T = 210$ in the numerical simulation with dimensionless parameters listed in Table I. Colors represent the velocity magnitude; red and blue represent positive and negative velocities, respectively. The dashed white circle represents the initial shape of the emulsion. (a) The vertical velocity U_z . (b) The azimuthal velocity U_θ . The secondary flows, which are denoted by the arrows in (b), drive the oil droplets to move from the valleys towards the peaks along the bottom layer of the flow cell and then upwards, hence enhancing the fingering.

late times, the vertical velocity at the emulsion front at the valley was downward, while that at the peak was upward. The emulsion at the peak was carried by the upward flow to the upper half of the Hele-Shaw cell and then brought inward by the backflow [39].

In order to understand the secondary flow, we establish a dimensionless depth-averaged flow model. We denote the total velocity \mathbf{U} as the sum of the horizontal velocity $\mathbf{V}(R, \theta, Z, T)$, i.e., the velocity in the (R, θ) plane, and the vertical velocity $U_z(R, \theta, Z, T)\mathbf{e}_z$, which is written as

$$\mathbf{U} = \mathbf{V}(R, \theta, Z, T) + U_z(R, \theta, Z, T)\mathbf{e}_z. \quad (14)$$

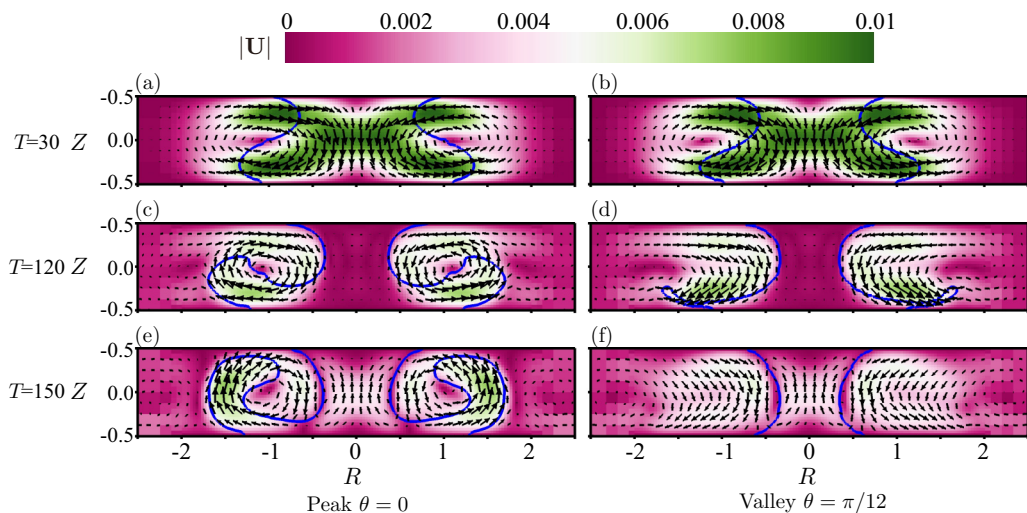


FIG. 5. Time evolution of the velocity field (arrows) and the emulsion/water boundary (blue curve), i.e., $\Phi = 1$, in vertical cross sections through the origin (R, Z plane) in the numerical simulation (a, c, e) at the peak $\theta = 0$ and (b, d, f) at the valley $\theta = \pi/12$, at $T = 30, 120$, and 210 . Dimensionless parameters are listed in Table I. The size of the arrows and the background color both represent the magnitude of the velocity.

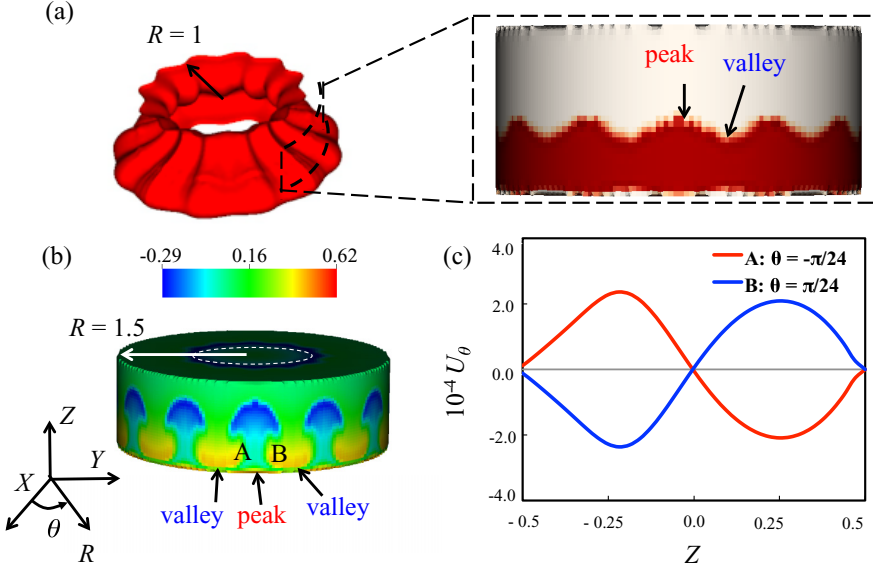


FIG. 6. Illustration of the mechanism of the instability. (a) Emulsion/water boundary $\Phi = 1$ in the numerical simulation, with dimensionless parameters listed in Table I, at $T = 30$ (left panel) and the cross section at $R = 1.5$ (right panel). The height of the emulsion is greater at the peaks than the valleys. (b) Density distribution at $R = 1.5$, $T = 210$, where green, yellow, and blue represent zero, positive, and negative velocities, respectively. The dashed white circle represents the initial shape of the emulsion. (c) Results of the numerical simulation of the azimuthal velocity U_θ as a function of Z at $R = 1.5$ and $T = 210$ at $\theta = -\pi/(2k)$ [red curve; also, point A in (b)] and $\theta = \pi/(2k)$ [blue curve; also, point B in (b)], where $k = 12$.

We derive the expression of the horizontal velocity as a cubic function of Z (see Appendix A) [39,41–43],

$$\mathbf{V} = -\frac{1}{6}(\beta_o\phi_0)^{-1}Z\left(Z - \frac{1}{2}\right)\left(Z + \frac{1}{2}\right)\nabla_{\text{hor}}^*\left(\frac{\bar{\rho}}{\rho_w}\right), \quad (15)$$

where $\bar{\rho}(R, \theta)$ is the depth-averaged density, and $\nabla_{\text{hor}}^* = \frac{\partial}{\partial R} + \frac{1}{R}\frac{\partial}{\partial \theta}$ is the gradient in the (R, θ) plane; for $\bar{\rho}$ independent of θ , the flow is purely radial. It can be seen from Eq. (15) that the horizontal velocity in the lower half of the flow cell, i.e., $\mathbf{V}|_{Z < 0}$, is in the opposite direction of the horizontal gradient of the depth-averaged fluid density $\nabla_{\text{hor}}^*(\bar{\rho}/\rho_w)$, while the direction is changed in the upper half of the flow cell. At late times when the salt diffuses horizontally away from the aqueous phase of the emulsion, the density of the emulsion becomes lower than the ambient fluid. The initial perturbation of the emulsion [see Fig. 1(d)] causes the height of the emulsion at the peaks to be larger than that at the valleys [see Fig. 6(a)], which causes an azimuthal density distribution [see Fig. 6(b)]. It is obvious that the depth-averaged density has an azimuthal distribution: the density at the peaks (more emulsion) is now lower than that at the valleys ($\bar{\rho}_{\text{peak}} < \bar{\rho}_{\text{valley}}$). This density distribution drives the horizontal velocity \mathbf{V} towards the peak at $Z < 0$ and towards the valley at $Z > 0$ [see Fig. 6(c)], which leads to the secondary flow shown in the numerical simulations reported in Fig. 5(b).

C. The criteria of the instability: The influences of $\alpha_{s,o}$ and $c_{\text{em}}/c_{\text{ext}}$

Given that there are two components, i.e., salt and oil, with opposite influences on the density of the fluid and significantly different diffusion coefficients, the instability is not guaranteed unless two criteria are satisfied: (i) The emulsion should be denser than the external fluid at the beginning; and

(ii) the emulsion should become less dense than the external fluid as time progresses. Specifically, the two criteria of the instability in our problem are given by

$$\alpha_{\text{ini}} \equiv \frac{\Delta\rho_{\text{em,ini}}}{\Delta\rho_{\text{ext}}} = \frac{c_{\text{em}}}{c_{\text{ext}}}(1 - \phi_0 - \alpha_{s,o}^{-1}) > 1, \quad (16a)$$

$$\alpha_{\text{final}} \equiv \frac{\Delta\rho_{\text{em,final}}}{\Delta\rho_{\text{ext}}} = 1 - \phi_0 - \alpha_{s,o}^{-1} < 1, \quad (16b)$$

where α_{ini} and α_{final} represent, respectively, the initial and final ratios of the density of the emulsion compared to the external fluid. Here, we assume that the volume of the Hele-Shaw cell is much larger than the volume of the emulsion, so that the salt concentration of the external fluid changes negligibly. Note that Eq. (16b) is always satisfied ($\phi_0 > 0$, $\alpha_{s,o} > 0$), so that the instability criteria reduce to Eq. (16a). Hence, we observe that two dimensionless parameters, $\alpha_{s,o}$ and $c_{\text{em}}/c_{\text{ext}}$, play roles in determining the stability of the flow.

The stability diagram with axes $\alpha_{s,o}$ and $c_{\text{em}}/c_{\text{ext}}$ is shown in Fig. 7(a), where both the experimental and the numerical results are compared with the hypothesized stability criterion [Eq. (16a)]. The results show that all of the experiments with stable results (blue circles) and numerical simulations with stable results (blue crosses) and unstable results (red crosses) lie in the regime expected by Eq. (16a). Most of the experiments with unstable results (red diamonds) agree with the prediction of Eq. (16a) except for one experiment with $\alpha_{s,o} = 4.9 \times 10^{-1}$ and $c_{\text{em}}/c_{\text{ext}} = 1.0 \times 10^2$ where mineral oil was used. The reason for the outlier might be that mineral oil was much less viscous than silicone oil so the oil droplets were smaller in the emulsion made with mineral oil rather than with silicone oil by the same ultrasonication process [44,45]. This would have led to a much higher oil volume fraction and much higher effective viscosity of the mineral oil emulsion, which might cause another instability related to viscosity gradients.

D. The growth rate of the instability and the most unstable mode: The influence of Pe_s

We conducted the simulations starting from an initial condition with different wave numbers; the oil volume fraction for an initial condition with a specific wave number k is denoted Φ_k . In order to quantify the azimuthal instability in a numerical simulation for the initial wave number k , we define the average azimuthal oil volume fraction as the integral of the oil volume fraction Φ_k across radius R and depth Z , given by

$$\Psi_k(\theta, T) \equiv \int_0^\infty \int_{-1/2}^{1/2} \Phi_k(R, Z, \theta, T) R dZ dR. \quad (17)$$

This definition corresponds to the average azimuthal oil distribution in the numerical simulations [see Figs. 3(d)–3(f)] and is also consistent with the azimuthal intensity distribution in the experimental images [see Figs. 3(a)–3(c)]. The instability is quantified by the amplitude of $\Psi_k(\theta, T)$, which is the difference between the values at the peaks, i.e., $\theta_p = 2n\pi/k$, and those at the valleys, i.e., $\theta_v = (2n+1)\pi/k$, where $n \in \{0, 1, \dots, k-1\}$. The amplitude of $\Psi_k(\theta, T)$ is given by

$$\Delta\Psi_k(T) = \Psi_k(\theta_p, T) - \Psi_k(\theta_v, T). \quad (18)$$

The time evolution of $\Delta\Psi_k(T)$ for $k = 3, 5, 12, 24$, and 48 in numerical simulations with dimensionless parameters listed in Table I is shown in Fig. 7(b). At very early times, the amplitude does not increase significantly because the initial condition is stably stratified. After salt has diffused sufficiently out of the spreading emulsion, the instability sets in, causing $\Delta\Psi_k(T)$ to grow. Since the horizontal axis T is linear, whereas the vertical axis $\Delta\Psi_k(T)$ is logarithmic, beyond an early-time transient, the amplitudes $\Delta\Psi_k(T)$ for different k values approximately follow an exponential relation in T ,

$$\Delta\Psi_k(T) \propto \exp(\sigma_k T), \quad (19)$$

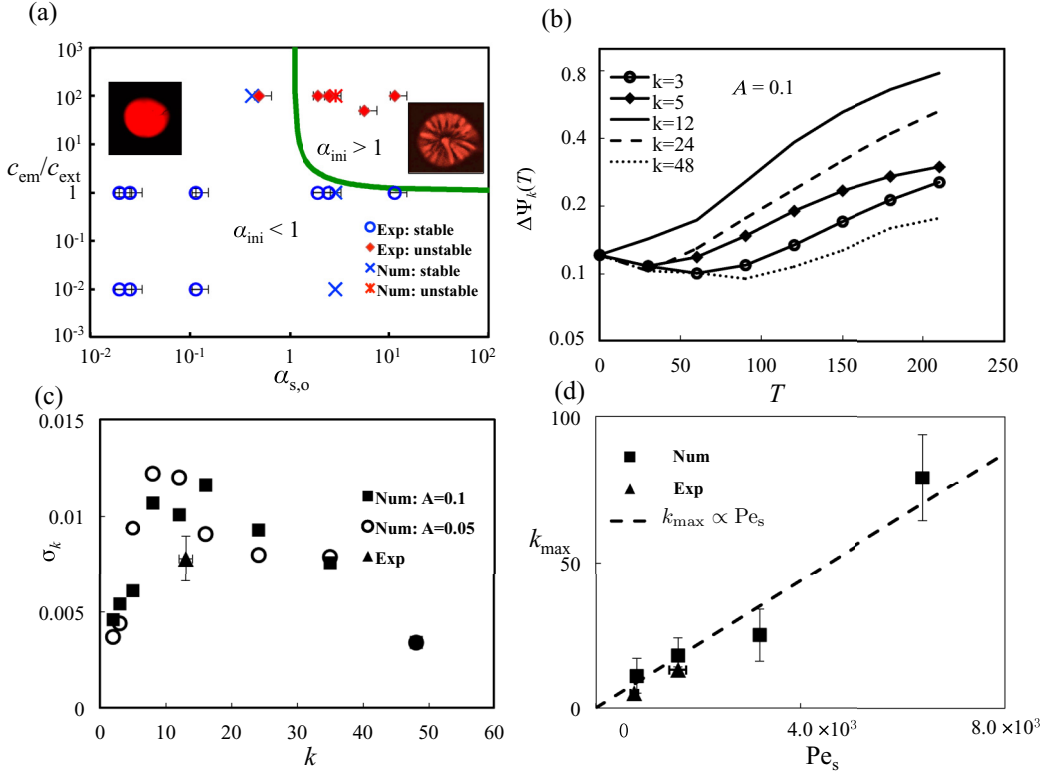


FIG. 7. Instability criteria, growth rate, and most unstable mode of the instability. (a) Stability diagram showing the effects of dimensionless parameters c_{em}/c_{ext} and $\alpha_{s,o}$, with other dimensionless parameters listed in Table I. When c_{em}/c_{ext} and $\alpha_{s,o}$ increase and α_{ini} [see Eq. (16a)] changes from below 1 to above 1, the results of both the experiments and the numerical simulation change from stable (blue circle and blue crosses) to unstable (red diamonds and red crosses). (b) Time evolution of the amplitude of the azimuthal oil volume fraction $\Delta\Psi_k(T)$ for $k = 3, 5, 12, 24$, and 48 in a numerical simulation with all other dimensionless parameters listed in Table I. (c) Growth rate of the instability σ_k versus azimuthal wave number k in numerical simulations with the amplitude of initial perturbations $A = 0.1$ (squares) and $A = 0.05$ (circles) and with all other dimensionless parameters listed in Table I. The growth rate of the dominant unstable mode in the experiment with $c_{em} = 100$ mM and $c_{ext} = 1$ mM is also denoted by the triangle (see Appendix B). (d) Dependence of the most unstable wave number k_{max} on Pe_s , with all other dimensionless parameters listed in Table I.

where σ_k is defined as the growth rate of the instability with wave number k . The results [see Fig. 7(b)] show that the modes with intermediate k grow fastest, whereas modes with small or large k grow more slowly. This suggests that there exists a most unstable mode k_{max} defined as the one with the maximum growth rate σ_k .

In order to determine the most unstable mode, the growth rate of the instability σ_k versus the azimuthal wave number k is shown in Fig. 7(c). The numerical simulations with the amplitudes of initial perturbations both $A = 0.1$ (squares) and $A = 0.05$ (circles) show that the most unstable mode $k_{max,num} \in [10, 20]$. The close data points for the amplitudes $A = 0.05$ and 0.1 indicate only a weak influence of the amplitude of the initial perturbations. The growth rate of the dominant, i.e., most unstable, mode in the experiment with $c_{em} = 100$ mM and $c_{ext} = 1$ mM is denoted by the blue triangle (see Appendix B). The most unstable mode in experiments was $k_{max,exp} = 12 \pm 1$, which agrees with the numerical results. The growth rate measured in the experiments was also close to that from the numerical simulations.

We now develop a scaling argument to show the dependence of k_{\max} on Pe_s , the Péclet number of salt. We consider the growth of perturbations with an azimuthal wave number k on a spreading current with characteristic radius $R(t)$. The time scale over which salt is advected across the wavelength of the perturbation $L_k = 2\pi R/k$ is $t_u^{(k)} \approx L_k/[gH^3 \Delta\rho/(12\mu_w R)]$. Meanwhile, azimuthal disturbances are smoothed out by diffusion over a time scale $t_D^{(k)} \approx L_k^2/D_s$. If the advection is fast ($t_u^{(k)} \ll t_D^{(k)}$), the compositions of both the emulsion and the surrounding liquid remain unchanged. This situation results in a stably spreading gravity current, as the spreading emulsion is always more dense than the surrounding liquid by virtue of containing more salt. By contrast, if the diffusion of salt is fast ($t_D^{(k)} \ll t_u^{(k)}$), azimuthal perturbations of the salt concentration relax exponentially before the emulsion has had time to advect. However, since the current also diffuses radially, axisymmetric modes of the concentration field remain and dominate the mode of instability.

Thus, in both the advection-dominated limit [small wave numbers, $k \ll gH^3 \Delta\rho/(12\mu_w D_s)$] and the diffusive limit [large wave numbers, $k \gg gH^3 \Delta\rho/(12\mu_w D_s)$], azimuthal structures are either stable or subdominant to an axisymmetric overturning instability. It stands to reason that the most unstable azimuthal mode corresponds to a balance between advection and diffusive transport, which yields the condition $k_{\max} \propto gH^3 \Delta\rho/(12\mu_w D_s) \sim \text{Pe}_s$. The most unstable modes k_{\max} obtained in experiments (red triangles) and numerical simulations (blue squares) are plotted versus Pe_s after fixing other dimensionless parameters in Fig. 7(d). Both experimental and numerical results demonstrate the roughly linear dependence of k_{\max} on Pe_s .

V. CONCLUSION

In this paper, we have shown experimentally that when a drop of an oil-in-water emulsion with a high salt concentration in its aqueous phase was injected into a Hele-Shaw cell filled with a salt solution of a low concentration, the drop spread and a flowerlike pattern of the emulsion appeared. We performed a large number of experiments varying the relative density difference and the ratio of the salt concentrations. We then conducted numerical simulations of this problem. The experimental and numerical results agree well both qualitatively and quantitatively for describing the main features of this pattern-forming instability. The numerical results confirm the hypothesis that the change in the fluid density caused by salt and oil is the key. Initially, the emulsion was denser than the ambient fluid, so it spread along the bottom of the cell. However, as it spread, salt, which diffused much more rapidly than the oil droplets, diffused from the droplet phase to the surrounding medium so that the drop finally became less dense than the ambient fluid. This transport introduced an unstable vertical density gradient. We also described the corresponding secondary flow, which was in the form of an azimuthal instability, by establishing a depth-averaged analytical model. The criterion for pattern formation, the growth rate of the instability, and the most unstable mode of the instability are also discussed here in terms of the dimensionless parameters.

The current work suggests the possibility of enhancing oil-water mixing by generating a salt gradient. For example, it has been observed that higher oil recovery can be obtained by flooding an oil reservoir containing high-salinity formation brine with low-salinity water, but the underlying mechanism is poorly understood [46–48]. Considering that the Reynolds number and the Péclet number are comparable between the current work and the oil reservoirs with large pore sizes, close to the height of the Hele-Shaw cell, e.g., sandstone and mudstone [49,50], the current work suggests a possible mechanism by which the vertical and horizontal instabilities induced by a salt gradient drive the oil from pores that are otherwise difficult to reach, which may help explain the enhanced oil recovery.

ACKNOWLEDGMENTS

We thank Dr. A. Perazzo for helpful advice on the surfactants. This work was supported by the NSF Chemo-Mechanical Assembly (Grant No. NSF-CCI-1740630) and funding from Charlotte Elizabeth Procter fellowships and the Mary and Randall Hack '69 Graduate Award at Princeton

University. L.Z. thanks the Swedish Research Council for a VR International Postdoctoral Grant (No. 2015-06334).

APPENDIX A: DEPTH-AVERAGED MODE

By assuming that $|U_Z| \ll |V|$ and inertia is negligible, the momentum equation, (10b), reduces to the stress balance

$$\frac{\partial P}{\partial Z} = -(\beta_o \phi_0 \text{Re})^{-1} \frac{\Delta \rho}{\rho_w}, \quad (\text{A1a})$$

$$\nabla_{\text{hor}}^* P = \text{Re}^{-1} \frac{\partial^2 V}{\partial Z^2}, \quad (\text{A1b})$$

where ∇_{hor}^* represents the gradient in the (R, θ) plane. We use the depth-averaged idea to further simplify Eqs. (A1). By writing the density $\Delta \rho$ as the sum of the depth-averaged density $\bar{\rho}$ and the deviation ρ' , i.e., $\Delta \rho(R, \theta, Z) = \bar{\rho}(R, \theta) + \rho'(R, \theta, Z)$, and assuming that $|\rho'| \ll |\bar{\rho}|$, we can integrate Eq. (A1a) and arrive at

$$P(R, \theta, Z) = P_0(R, \theta) - (\beta_o \phi_0 \text{Re})^{-1} Z \left(\frac{\bar{\rho}}{\rho_w} \right), \quad (\text{A2})$$

where $P_0(X, Y)$ is the pressure at $Z = 0$. By substituting Eq. (A2) into (A1b), integrating across the depth of the Hele-Shaw cell, and applying the no-slip boundary condition, $V(Z = \pm 1/2) = \mathbf{0}$, we obtain the expression of the horizontal velocity,

$$V(R, \theta, Z) = \text{Re} Z(Z-1) \nabla_{\perp}^* P_0 - \frac{1}{6} (\beta_o \phi_0)^{-1} Z \left(Z - \frac{1}{2} \right) \left(Z + \frac{1}{2} \right) \nabla_{\text{hor}}^* \left(\frac{\bar{\rho}}{\rho_w} \right). \quad (\text{A3})$$

By substituting Eq. (A3) into the continuity equation $\nabla_{\text{hor}}^* \cdot \mathbf{U} = 0$, integrating it across the depth of the Hele-Shaw cell, and applying the no-slip boundary condition that $\mathbf{U}(Z = \pm 1/2) = \mathbf{0}$, we find

$$\nabla_{\text{hor}}^* P_0(R, \theta) = 0. \quad (\text{A4})$$

Combining Eq. (A4) with boundary condition $P_0(R \rightarrow \infty) = P_{\infty}(T)$, we obtain a homogeneous pressure P_0 , which further simplifies Eq. (A3) to Eq. (15).

APPENDIX B: PROCESSING EXPERIMENTAL IMAGES

In order to extract the most unstable mode k_{\max} , i.e., the mode with the maximum growth rate σ_k , we processed the experimental images of the top views of the emulsion patterns [see Figs. 3(a)–3(c)] in the following steps. First, the images were imported into MATLAB and converted to black-and-white formats. This yielded an $N_x \times N_y$ intensity matrix I , with element $I(i, j)$ representing the intensity of the pixel in the i th row and j th column. To extract the background, the pixels with intensity $I(i, j)$ lower than a threshold were set to equal 0. The center of the pattern (x_c, y_c) was determined manually. Next, we calculated the azimuthal intensity $\langle I \rangle_{\theta}$ sampled on $\theta = n\pi/180$ with $n = 0, 1, \dots, 359$ by

$$\langle I \rangle_{\theta} = \sum_{r \in Z^+ \cap D} r I(r \cos \theta + x_c, r \sin \theta + y_c), \quad (\text{B1})$$

where $I(r \cos \theta + x_c, r \sin \theta + y_c)$ was obtained by two-dimensional interpolation, and D is the group of r satisfying

$$0 \leq r \cos \theta + x_c \leq N_x - 1, \quad (\text{B2a})$$

$$0 \leq r \sin \theta + y_c \leq N_y - 1. \quad (\text{B2b})$$

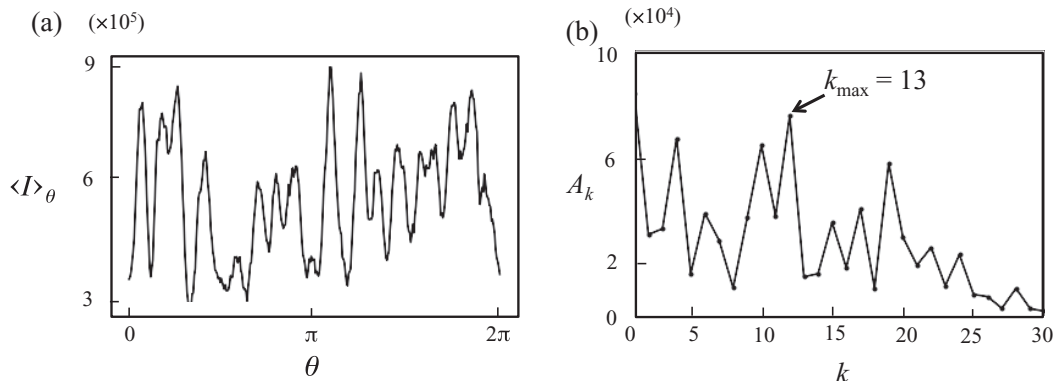


FIG. 8. Results of processing the experimental image in Fig. 3(c). (a) Azimuthal intensity $\langle I \rangle_\theta$ as a function of θ in Fig. 3(c). (b) Result of the Fourier transform of $\langle I \rangle_\theta$.

The azimuthal intensity $\langle I \rangle_\theta$ as a function of θ in Fig. 3(c) is shown in Fig. 8(a) with obvious intensity peaks that correspond to the fingers in Fig. 3(c). The most unstable mode k_{\max} was extracted by Fourier transforming the azimuthal intensity $\langle I \rangle_\theta$. The result of Fourier transform is shown in Fig. 8(b): the most unstable mode $k_{\max} = 12$ with maximum amplitude A_k is denoted by the arrow. The higher modes with lower amplitudes are not shown here. The dimensionless growth rate σ_k of the most unstable mode k_{\max} is determined in terms of the amplitude $A_{k_{\max}}$ by

$$A_{k_{\max}}(t) \propto \exp(\sigma_k t / t_c), \quad (\text{B3})$$

where $A_{k_{\max}}(t)$ is the amplitude of the most unstable mode $k_{\max} = 12$ at time t .

-
- [1] P. Bergé and M. Dubois, Rayleigh-Bénard convection, *Contemp. Phys.* **25**, 535 (1984).
 [2] M. C. Cross and P. C. Hohenberg, Pattern formation outside of equilibrium, *Rev. Mod. Phys.* **65**, 851 (1993).
 [3] G. M. Whitesides and B. Grzybowski, Self-assembly at all scales, *Science* **295**, 2418 (2002).
 [4] G. Feingold, I. Koren, H. Wang, H. Xue, and W. A. Brewer, Precipitation-generated oscillations in open cellular cloud fields, *Nature* **466**, 849 (2010).
 [5] H. Hasegawa, A. Retinò, A. Vaivads, Y. Khotyaintsev, M. André, T. K. M. Nakamura, W.-L. Teh, B. U. Ö. Sonnerup, S. J. Schwartz, Y. Seki, M. Fujimoto, Y. Saito, H. Rème, and P. Canu, Kelvin-Helmholtz waves at the Earth's magnetopause: Multiscale development and associated reconnection, *J. Geophys. Res. Space Phys.* **114**, A12207 (2009).
 [6] K. Tsuchiya, The clouds with the shape of Kármán vortex street in the wake of Cheju Island, Korea, *J. Meteor. Soc.* **47**, 457 (1969).
 [7] L. V. Zhang, P. Brunet, J. Eggers, and R. D. Deegan, Wavelength selection in the crown splash, *Phys. Fluids* **22**, 122105 (2010).
 [8] S. M. Troian, E. Herbolzheimer, S. A. Safran, and J. F. Joanny, Fingering instabilities of driven spreading films, *Europhys Lett.* **10**, 25 (1989).
 [9] D. E. Kataoka and S. M. Troian, A theoretical study of instabilities at the advancing front of thermally driven coating films, *J. Colloid Sci.* **192**, 350 (1997).
 [10] N. Xue, S. Khodaparast, L. Zhu, J. Nunes, H. Kim, and H. A. Stone, Laboratory layered latte, *Nat. Commun.* **8**, 1960 (2017).

- [11] T. B. Jones, Electrohydrodynamically enhanced heat transfer in liquids—A review, *Adv. Heat Transfer* **14**, 107 (1979).
- [12] L. Paterson, Radial fingering in a Hele-Shaw cell, *J. Fluid Mech.* **113**, 513 (1981).
- [13] G. M. Homsy, Viscous fingering in porous media, *Annu. Rev. Fluid Mech.* **19**, 271 (1987).
- [14] T. T. Al-Housseiny, P. A. Tsai, and H. A. Stone, Control of interfacial instabilities using flow geometry, *Nat. Phys.* **8**, 747 (2012).
- [15] J. Kim, F. Xu, and S. Lee, Formation and Destabilization of the Particle Band on the Fluid-Fluid Interface, *Phys. Rev. Lett.* **118**, 074501 (2017).
- [16] H. S. Rabbani, D. Or, Y. Liu, C.-Y. Lai, N. B. Lu, S. S. Datta, H. A. Stone, and N. Shokri, Suppressing viscous fingering in structured porous media, *Proc. Natl. Acad. Sci. USA* **115**, 4833 (2018).
- [17] C. W. MacMinn, J. A. Neufeld, M. A. Hesse, and H. E. Huppert, Spreading and convective dissolution of carbon dioxide in vertically confined, horizontal aquifers, *Water Resour. Res.* **48**, W11516 (2012).
- [18] A. C. Slim, M. M. Bandi, J. C. Miller, and L. Mahadevan, Dissolution-driven convection in a Hele-Shaw cell, *Phys. Fluids* **25**, 024101 (2013).
- [19] H. E. Huppert and J. A. Neufeld, The fluid mechanics of carbon dioxide sequestration, *Annu. Rev. Fluid Mech.* **46**, 255 (2014).
- [20] R. S. J. Sparks, R. T. Bonnecaze, H. E. Huppert, J. R. Lister, M. A. Hallworth, H. Mader, and J. Phillips, Sediment-laden gravity currents with reversing buoyancy, *Earth Planet. Sci. Lett.* **114**, 243 (1993).
- [21] A. J. Hogg, H. E. Huppert, and M. A. Hallworth, Reversing buoyancy of particle-driven gravity currents, *Phys. Fluids* **11**, 2891 (1999).
- [22] C. Diddens, H. Tan, P. Lv, M. L. Versluis, J. G. M. Kuerten, X. Zhang, and D. Lohse, Evaporating pure, binary and ternary droplets: Thermal effects and axial symmetry breaking, *J. Fluid Mech.* **823**, 470 (2017).
- [23] M. L. Szulczewski and R. Juanes, The evolution of miscible gravity currents in horizontal porous layers, *J. Fluid Mech.* **719**, 82 (2013).
- [24] J. S. Turner, Double-diffusive phenomena, *Annu. Rev. Fluid Mech.* **6**, 37 (1974).
- [25] H. E. Huppert and J. S. Turner, Double-diffusive convection, *J. Fluid Mech.* **106**, 299 (1981).
- [26] H. E. Huppert and R. S. J. Sparks, Double-diffusive convection due to crystallization in magmas, *Annu. Rev. Earth Planet Sci.* **12**, 11 (1984).
- [27] K. R. Sreenivas, O. P. Singh, and J. Srinivasan, On the relationship between finger width, velocity, and fluxes in thermohaline convection, *Phys. Fluids* **21**, 026601 (2009).
- [28] T. Radko, *Double-Diffusive Convection* (Cambridge University Press, Cambridge, UK, 2013).
- [29] E. Keowmaneechai and D. J. McClements, Effect of CaCl₂ and KCl on physiochemical properties of model nutritional beverages based on whey protein stabilized oil-in-water emulsions, *J. Food Sci.* **67**, 665 (2002).
- [30] D. J. McClements, Protein-stabilized emulsions, *Curr. Opin. Colloid Interface Sci.* **9**, 305 (2004).
- [31] V. Vitagliano and P. A. Lyons, Diffusion coefficients for aqueous solutions of sodium chloride and barium chloride, *J. Am. Chem. Soc.* **78**, 1549 (1956).
- [32] C. C. Miller, The Stokes-Einstein law for diffusion in solution, *Proc. R. Soc. London A* **106**, 724 (1924).
- [33] See Supplemental Material at <http://link.aps.org/supplemental/10.1103/PhysRevFluids.4.084307> for a three-dimensional video of the emulsion pattern formation observed using a confocal microscope (Nikon A1R HD) and postprocessing with NIS Element Viewers.
- [34] S. Popinet, BASILISK web page; <http://basilisk.fr>.
- [35] C. J. Sanders and J. P. Holman, Franz Grashof and the Grashof number, *Int. J. Heat Mass Transf.* **15**, 562 (1972).
- [36] R. B. Bird, E. N. Lightfoot, and E. W. Stewart, *Transport Phenomenon* (Wiley, New York, 2007).
- [37] T. L. Bergman, F. P. Incropera, D. P. DeWitt, and A. S. Lavine, *Fundamentals of Heat and Mass Transfer* (John Wiley & Sons, New York, 2011).

- [38] See Supplemental Material at <http://link.aps.org/supplemental/10.1103/PhysRevFluids.4.084307> for a three-dimensional video of the emulsion/aqueous boundary in a numerical simulation with parameters listed in Table I.
- [39] B. Selva, L. Daubersies, and J. B. Salmon, Solutal Convection in Confined Geometries: Enhancement of Colloidal Transport, *Phys. Rev. Lett.* **108**, 198303 (2012).
- [40] Z. Zheng, B. Guo, I. C. Christov, M. A. Celia, and H. A. Stone, Flow regimes for fluid injection into a confined porous medium, *J. Fluid Mech.* **767**, 881 (2015).
- [41] R. V. Birikh, Thermocapillary convection in a horizontal layer of liquid, *J. Appl. Mech. Tech.* **7**, 43 (1966).
- [42] C. Loussert, A. Bouchaudy, and J. B. Salmon, Drying dynamics of a charged colloidal dispersion in a confined drop, *Phys. Rev. Fluids* **1**, 084201 (2016).
- [43] C. J. Van Duijn and R. J. Schotting, The interface between fresh and salt groundwater in horizontal aquifers: The Dupuit–Forchheimer approximation revisited, *Transport Porous Med.* **117**, 481 (2017).
- [44] J. T. Davies, A physical interpretation of drop sizes in homogenizers and agitated tanks, including the dispersion of viscous oils, *Chem. Eng. Sci.* **42**, 1671 (1987).
- [45] A. Gupta, H. B. Eral, T. A. Hatton, and P. S. Doyle, Controlling and predicting droplet size of nanoemulsions: Scaling relations with experimental validation, *Soft Matter* **12**, 1452 (2016).
- [46] S. Bagci, M. V. Kok, and U. Turksoy, Effect of brine composition on oil recovery by waterflooding, *Petrol. Sci. Technol.* **19**, 359 (2001).
- [47] J. J. Sheng, Critical review of low-salinity waterflooding, *J. Pet. Sci. Eng.* **120**, 216j (2014).
- [48] M. D. Jackson, J. Vinogradov, G. Hamon, and M. Chamerois, Evidence, mechanisms and improved understanding of controlled salinity waterflooding. Part 1: Sandstones, *Fuel* **185**, 772 (2016).
- [49] L. M. Anovitz and D. R. Cole, Characterization and analysis of porosity and pore structures, *Rev. Mineral. Geochem.* **80**, 61 (2015).
- [50] W. B. Bartels, M. Rücker, S. Berg, H. Mahani, A. Georgiadis, N. Brussee, A. Coorn, H. van der Linde, A. Fadili, C. Hinz, and A. Jacob, Micro-CT study of the impact of low salinity waterflooding on the pore-scale fluid distribution during flow, in *International Symposium of the Society of Core Analysts, Snowmass, CO* (2016).